Investigating the $\chi^{(3)}$ Nonlinearity of a Josephson Junction Array for Travelling-Wave Parametric Amplification in the W-band

Javier Navarro Montilla, Ryan C. Stephenson, Arnaud Barbier, Nikita Klimovich, Yves Bortolotti, Eduard F. C. Driessen, Peter K. Day, and Boon-Kok Tan

***Abstract*—At microwave frequencies, Josephson junction arrays have been widely employed to create metamaterials exhibiting a third-order ($\chi^{(3)}$) nonlinearity, analogous to the Kerr effect in optics. These nonlinear metamaterials enable parametric amplification, as in Josephson Travelling-Wave Parametric Amplifiers (JTWPAs), which achieve quantum-limited noise performance over multi-gigahertz bandwidths. The exceptional properties of JTWPAs make them ideal for the sensitive readout of weak microwave signals, with applications in quantum computing, astrophysics, and fundamental physics experiments. Extending JTWPAs to higher frequencies, such as the W-band (70–110 GHz), holds promise for first-stage amplification in astronomical receivers, lowering system noise; as well as for reading out emerging superconducting qubit architectures at these frequencies. In this work, we investigate the $\chi^{(3)}$ nonlinear properties of Josephson arrays operating in the W-band as a step toward realising parametric gain at these frequencies. We designed and fabricated an array composed of 704 Nb/Al-AlO_x/Nb tunnel junctions and experimentally demonstrated four-wave mixing via idler tone generation, providing clear evidence of third-order nonlinearity. These results mark an important step toward novel millimetre-wave and sub-millimetre-wave parametric-amplifier-based receiver technologies.**

***Index Terms*—Josephson junction, Metamaterial, Millimetre wave, Parametric Amplification, Travelling Wave.**

I. Introduction

The nonlinear properties of Josephson junctions have been widely exploited for application ranging from microwave to terahertz (THz) frequencies [1]. In the microwave regime, Josephson junctions constitute the building-block for many important applications, e.g., the voltage standard [2] and low-noise parametric amplifiers. The latter is a critical component for many ultra-sensitive physics experiments and instruments. Josephson Parametric Amplifiers (JPA), based on resonant circuits, have demonstrated quantum-limited noise performance [3], and have been widely used in quantum computing platforms for the single-shot readout of superconducting qubits [4]–[6], boosting the signal-to-noise ratio (SNR) of the system. Recently, the quest for larger JPA dynamic ranges has prompted the use of Josephson arrays, diluting the Kerr-type nonlinearity and hence increasing the compression point [7]. Despite their dynamic range improvement, JPAs suffer from limited bandwidth, in the order of $\sim 10 - 600$ MHz [8], due to the high-quality factor (Q-factor) resonant circuit needed to increase the signal interaction with the nonlinear inductance of the Josephson junctions [9].

Travelling Wave Parametric Amplifiers (TWPAs) solve the resonant paradigm of the JPAs by unfolding the nonlinear medium into a long transmission line made of either high-kinetic-inductance films (KTWPA) [10] or Josephson-junction array (JTWPAs) [11]. JTWPAs can be constructed by cascading bare Josephson junctions or Superconducting Quantum Interference Devices (SQUIDs) [12], [13]. When bare Josephson junctions or DC-SQUIDs are used, the quadratic current-dependent inductance of the individual junctions results in a third-order $\chi^{(3)}$ nonlinearity in the array. Therefore, if a strong pump tone (ω_p) co-propagates with a small signal tone (ω_s) in the JTWPA, a four-wave mixing process yields exchange of energy between the pump and the signal, resulting in the amplification of the signal tone at the output of the transmission line. An idler tone at frequency $\omega_\mathrm{i} = 2\omega_\mathrm{p} - \omega_\mathrm{s}$ is generated in this process to conserve energy and momentum of the system.

The quantum-limited noise and the broadband (in the order of several GHz in the microwave regime) performance demonstrated by TWPAs [11], [14], [15] have recently excited interest in numerous research fields. TWPAs have been successfully implemented for the readout of multiplexed qubit arrays [16], easing the path for quantum computing scalability. They have also been suggested and recently implemented for axion-like dark matter search experiments [17]–[19] and the readout of astronomical receivers [20], [21]. Furthermore, TWPAs have been an enabling technology for many fundamental physics experiments and concepts, e.g., the detection of spontaneous photon decay [22], generation of broadband squeezed light [23], [24] and microwave quantum radar applications [25].

In addition to their applications in the microwave regime, this technology could find a broad range of applications at higher frequencies. The millimetre (mm) and sub-mm wavelengths (30 GHz to 3 THz) are key astronomical windows that probe cold interstellar medium and enabling the imaging of astronomical sources such as black holes' event horizons, among others. TWPAs therefore could be used as the first stage ultra-low noise amplifier for these astronomical receivers,

Javier Navarro Montilla, Nikita Klimovich and Boon-Kok Tan are with the Department of Physics (Astrophysics), University of Oxford, Denys Wilkinson Building, Keble Road OX1 3RH, Oxford, UK. Arnaud Barbier, Yves Bortolotti and Eduard F. C. Driessen are with the Institut de Radioastronomie Millimétrique (IRAM), Saint Martin d'Hères, 38406, France. Ryan C. Stephenson and Peter K. Day are with the Jet Propulsion Laboratory, California Institute of Technology, Pasadena, CA 91109, USA. Javier Navarro Montilla is now with the National Quantum Computing Centre (NQCC), Rutherford Appleton Laboratory, Harwell Campus, Didcot, OX11 0QX.

Manuscript received May xx, 2025; revised May xx, 2025.

improving the system noise temperature by at least a factor of ∼5 [26]. This translates to doubling the system sensitivity and 4× increase in the observation speed, with a potential larger impact in the THz range.

Beyond astronomy, at frequencies higher than microwaves, superconducting qubits could operate at temperatures above 1 K and reduce the energy gap for signal conversion to optical frequencies, facilitating the quantum computer scalability. As a result, novel approaches to qubits operating in the W-band (ranging from 75-110 GHz) have been suggested using high kinetic inductance nano-wires [27], and recently demonstrated using Nb/Al-AlO_x/Nb junctions [28].

KTWPAs have been demonstrated to operate at frequencies higher than microwaves [29], [30]. However, there is a lack of exploration for JTWPA operation at these frequencies, which could leverage the extended superconductor-insulator-superconductor (SIS) tunnel junction fabrication infrastructures, making this technology more accessible to the scientific community. Moreover, this development could enable the on-chip integration of JTWPAs with SIS mixers, reducing interconnect losses and enhancing overall receiver performance.

As a foundational step toward realising JTWPAs in the W-band, this work investigates the $\chi^{(3)}$ nonlinear properties of a junction array specifically designed for operation around 90 GHz. We begin by outlining the key considerations for extending JTWPA operation beyond the microwave regime, which inform the design of our junction array. The device comprises 704 junctions fabricated using standard niobium/aluminium-aluminium-oxide/niobium (Nb/Al–AlO_x/Nb) trilayer tunnel junction technology. We present both DC and RF characterisations of the array at cryogenic temperatures, and discuss the implications of our results for future applications in parametric amplification and beyond.

II. Josephson Array Design

JTWPAs are formed by cascading a series of unit cells comprising one or more nonlinear components, such as bare Josephson junctions, creating a nonlinear superconducting transmission line (STL). The current-dependent (I) nonlinear inductance of the Josephson junction can be written as[1]:

$$L(I) = L_{\mathrm{j}} \left[1 + \frac{1}{2} \left(\frac{I}{I_*} \right)^2 \right] \tag{1}$$

where L_{j} is the intrinsic inductance of the junction defined as $L_{\mathrm{j}} = \frac{\phi_0}{I_*}$, where ϕ_0 is the reduced magnetic flux quantum and I_* set the scale of the nonlinearity and is equal to the critical current of the junction (I_{c}).

This nonlinear inductance, at the origin of the $\chi^{(3)}$ nonlinearity in the JTWPA, leads to a current-dependent phase shift for electromagnetic waves propagating through the STL, which can degrade gain and bandwidth if uncorrected. To compensate for this phase mismatch and improve gain, dispersion engineering techniques are employed to modify the line's dispersion relation locally. Two common approaches are resonant phase matching (RPM) — which introduces shunted LC resonators periodically along the line — and impedance loading, where the line's impedance is periodically modulated. A schematic of a JTWPA implementing RPM is shown in Fig. 1(a).

[1]This expression consists of an approximation based on a second-order Taylor expansion for $I/I_* \ll 1$, which estimates the inductance to a relative error $< 5\%$ up to $I/I_* \approx 0.6$.

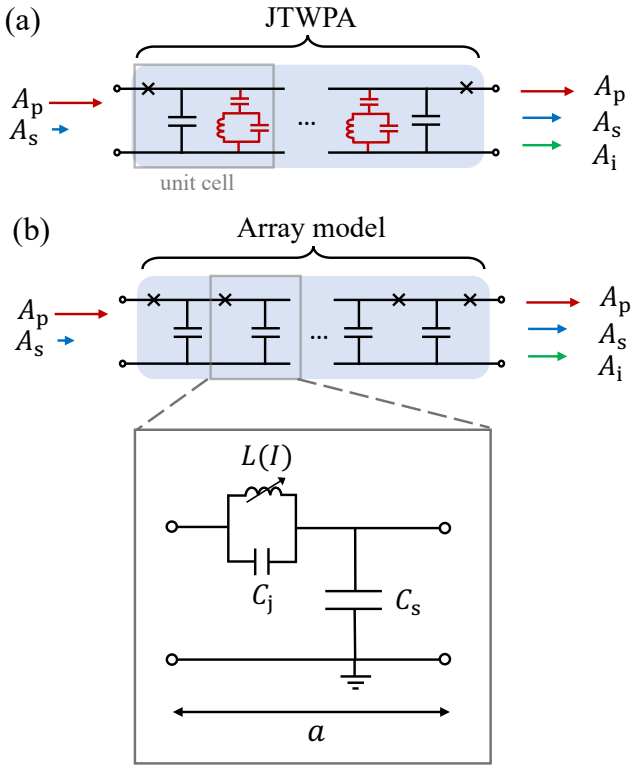

Fig. 1. (a) Circuit diagram of a JTWPA and its operational principle. An input strong pump (A_{p}) and a weak signal (A_{s}) tone propagate in the JTWPA resulting in signal gain and the generation of an idler (A_{i}) tone. Ground-shunted LC resonators (red) are added for Resonant Phase Matching (RPM). (b) Josephson junction array model used in our analysis. The zoom-in shows the unit cell, where a, C_{s}, C_{j} and L correspond to the physical length, the shunt capacitance to the ground, the junction capacitance and nonlinear inductance per unit cell respectively.

While dispersion engineering significantly improves gain and bandwidth, it does not affect the fundamental frequency limitations of the JTWPA. Therefore, to investigate these limitations, we adopt a simplified junction array model that captures the essential physical behaviour of the metamaterial medium. As shown in Fig. 1(b), each unit cell in this model consists of a junction capacitance C_{j}, a junction nonlinear inductance $L(I)$, and a shunt capacitance to ground C_{s}, which arises from the geometry of the transmission line.

A. Design considerations for W-band operation

We start the design process by identifying factors that may limit the operation of a junction array in the W-band, which firstly relate to the superconducting gap frequency (f_Δ) of the tunnel junction; since photons with frequency $f > f_\Delta$ will break the Copper pairs, and hence the superconducting state. Most of the recent JTWPAs use aluminium junctions [12], [13], [31], leveraging the maturity of this technology for qubit

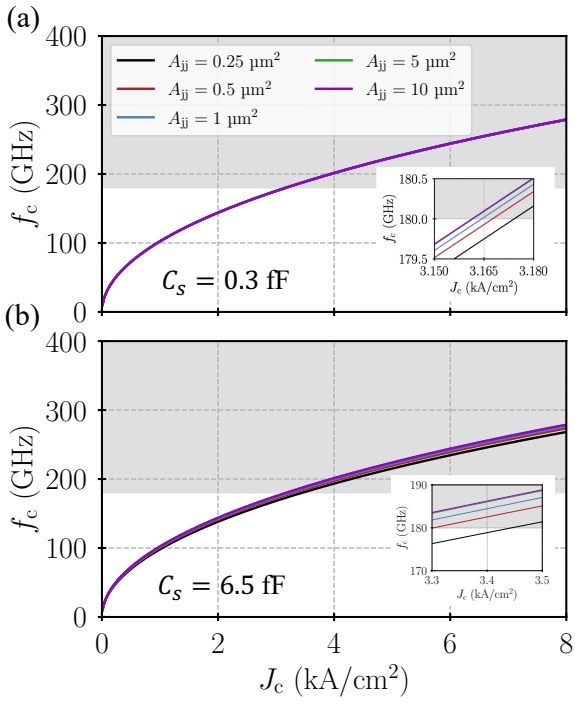

Fig. 2. (a) Cutoff frequency (f_c) of a junction array plotted against the critical current density of the junctions (J_c) for different junction's area (A_{jj}), with a shunt capacitance value of $C_s = 0.3$ fF and (b) $C_s = 6.5$ fF. A cutoff frequency higher than twice the operation frequency of our device i.e., $f_c > 180$ GHz, is shaded in grey. Insets shows the zoom-in plots focusing on range near 180 GHz.

applications. However, the low gap frequency of aluminium ($f_\Delta \approx 90$ GHz) limits its application to the microwave regimes. For operation in the W-band, we opt to use Nb/Al-AlO_x/Nb junctions, where $f_\Delta \approx 680$ GHz and their trilayer fabrication technique has been largely matured in the past decades.

Numerous JTWPAs implementations make use of silicon dioxide (SiO_2) parallel plate capacitors [11] or inverted microstrip with an aluminium oxide (Al_2O_3) dielectric layer [12], [13] to increase C_s, and thus match the device to the 50 Ω environment. These dielectric materials exhibit frequency-dependent losses, with reported loss tangent values up to $\tan\delta \sim 6 \cdot 10^{-3}$ [32]. Therefore, we opt for a coplanar waveguide (CPW) geometry for our array to avoid the use of lossy dielectric materials. Furthermore, operating our device in the W-band means that we are not confined to a 50 Ω environment, since the device will be mounted in a waveguide environment with waveguide-to-CPW transitions that generally have higher characteristic impedance around 100 Ω. This reduce the required C_s value, allowing us to utilise interdigitated capacitors, which do not need any dielectric layer.

Finally, the cutoff frequency (f_c) of the junction array forming the JTWPA will also determine the upper frequency limit[2] [33]: $\omega_c = 2\omega_0 \Big/ \sqrt{1 + 4\frac{\omega_0^2}{\omega_j^2}}$, where $\omega_0 = 1/\sqrt{L_j C_0}$ is the cutoff frequency of the STL and $\omega_j = 1/\sqrt{L_j C_j}$ is the plasma frequency of the junctions. Both L_j and C_j are correlated and is dependent on the critical current density (J_c) and the size (A_{jj}) of the junction. In Fig. 2(a), we plot f_c as a function of J_c for different values of A_{jj}, with C_s fixed at 0.3 fF to account for the shunt capacitance of a CPW with approximately 2 µm gap (value obtained from Sonnet® [34]). As can be seen, f_c increases with J_c as expected, since L_j decreases with J_c resulting in an increased ω_j. On the other hand, A_{jj} has a negligible effect on f_c as the junction plasma frequency is dominating for small values of C_s. In this scenario, $L_j \propto 1/A_{jj}$, and $C_j \propto A_{jj}$, they therefore counterbalance the effect of A_{jj}.

The nonlinear inductance in JTWPAs also leads to the generation of unwanted harmonics and intermodulation products, limiting the desired wave-mixing process that underpins signal amplification. In microwave implementations, these spurious signals are often naturally suppressed by the strong dispersion near the cutoff frequency of the device. We adopt a similar strategy in our junction array design. Since our target operational band is centered around $f_0 = 90$ GHz (within the W-band), we set the cutoff frequency to $f_c = 2f_0 = 180$ GHz. This choice helps suppress higher-order harmonics and intermodulation products, therefore avoiding pump depletion and potential Copper pair breaking in the material. From Fig. 2(a), we reach this value with $J_c \approx 3.16$ kA/cm^2. However, assuming $A_{jj} = 0.5$ µm^2, the small C_s value results in $Z_0 \approx 300$ Ω, complicating the design of a waveguide-to-CPW transition[3]. As shown in Fig. 2(b), increasing the shunt capacitance to $C_s = 6.5$ fF, would allow us to reduce the characteristic impedance to $Z_0 = 70$ Ω for the same A_{jj} with $J_c \approx 3.4$ kA/cm^2, while still maintaining $f_c = 180$ GHz. This not only eases the design of the waveguide-to-CPW transition, but also reduces the phase-velocity of the array, further reducing the number of junctions required to achieve signal gain. Therefore, we fix the junctions parameters for our design to $J_c \approx 3.4$ kA/cm^2, $A_{jj} = 0.5$ µm^2, and $C_s = 6.5$ fF.

B. Gain simulation and coupling strategy

To convert the electrical parameters into physical dimensions, we use the 3D electromagnetic simulator Ansys® HFSS [36] to ensure an accurate representation of the electromagnetic behaviour of the STL. The unit cell model of our device is shown in Fig. 3(a). The length of the interdigitated stub capacitors of the CPW is optimised to reach $Z_0 = 70$ Ω, with $C_s \approx 6.5$ fF. We further added equipotential ground bridges to suppress the potential generation of slotline mode at high frequencies. The topology of our device incorporates a 400 nm Nb bottom layer, with a 200 nm SiO_2 spacer layer separating the bottom and the top Nb layer (400 nm). Both Nb layers are connected through a pair of 0.5 µm^2 junctions

[2]A more exhaustive model could include a geometrical inductance in series with the junction.

[3]Larger junctions result in smaller L_j and therefore would also require a larger number of junctions to reach the same gain in a JTWPA.

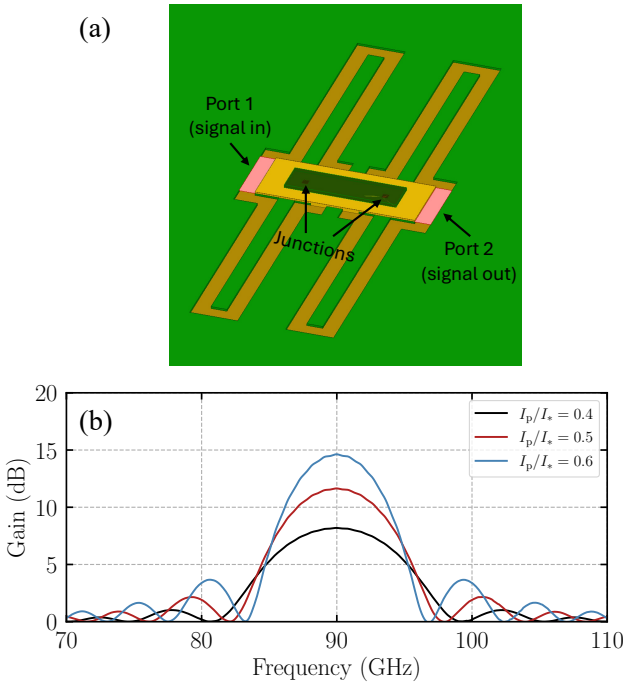

Fig. 3. (a) Layout of our device unit cell modelled in HFSS, showing the bottom layer (light green), spacer (yellow), top layer (dark green) and the junctions (red). The pink 2-D structures represent the input and output port in the HFSS model. (b) Simulated gain curve following the techniques in [35] for a 704-junctions array when pumped at three different levels of pump power over critical current I_p/I_*.

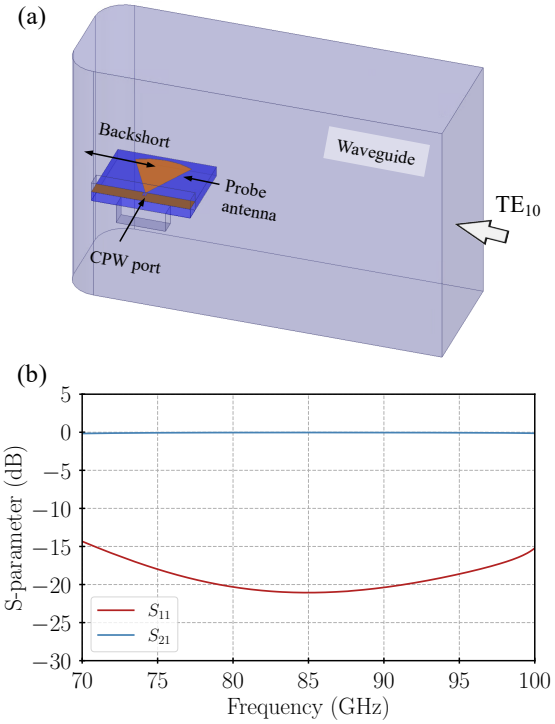

Fig. 4. (a) The probe antenna design modelled in HFSS including the WR-10 rectangular wavaguide and the backshort. The geometry is optimised to maximise the coupling in the W-band. (b) Simulation results of the transmission (blue) and return loss (red) for the probe antenna matched to a $Z_0 = 70\,\Omega$ CPW port. The return loss is kept below -15 dB from 70 to 100 GHz.

with $L_j = 19.4$ pH and $C_j = 37.6$ fF. The S-parameter of the simulated unit cell is cascaded 352 times (704 junctions in total) to form the entire array. Despite not implementing dispersion engineering techniques, our array holds the potential to generate usable signal gain when applying a pump tone at 90 GHz. To simulate the expected gain, we extract the propagation constant relation of the STL and solve the coupled-mode equations following the technique presented in [35]. The results for different pump power (I_p) values are plotted in Fig. 3(b). With this design, we expect reaching a signal gain of ~ 15 dB with $I_p/I_* = 0.6$ and a bandwidth of ~ 10 GHz.

For operation in W-band, we have to mount our device in a WR-10 waveguide environment, instead of interfacing with the commonly used microwave connectors. To achieve this, we need to couple the TE_{10} mode propagating in the waveguide into our CPW chip. This transition can be realised using a probe antenna. Using Ansys HFSS, we simulate a Nb probe antenna on a 100 µm thick high-resistive silicon substrate, and we optimise the geometry (Fig. 4(a)) to maximise power coupling in the W-band range while matching the output impedance of the probe antenna to $Z_0 = 70\,\Omega$. Fig. 4(b) shows the S_{21} and S_{11} simulated, where the return loss is less than –15 dB from 70 GHz to 100 GHz. A pair of these antennas is then connected to the input and output ports of the array to couple the energy from the input waveguide to the chip, and from the chip to the output waveguide.

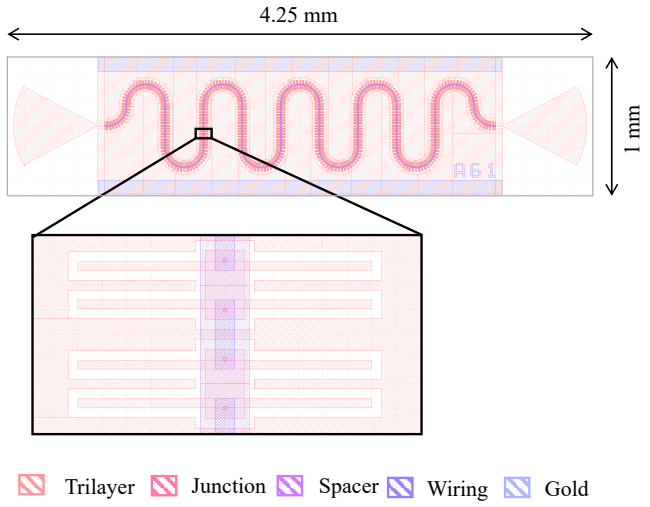

Fig. 5. Layout of the JTWPA showing a meandered STL structure to reduce the size of the chip and therefore eliminate possible resonant modes in the substrate.

III. Device Fabrication and Screening

The layout of the Josephson array chip with the probe antennas is presented in Fig. 5, which has a meandered transmission line geometry to reduce the chip size, and hence suppress the generation of resonant modes in the substrate within the

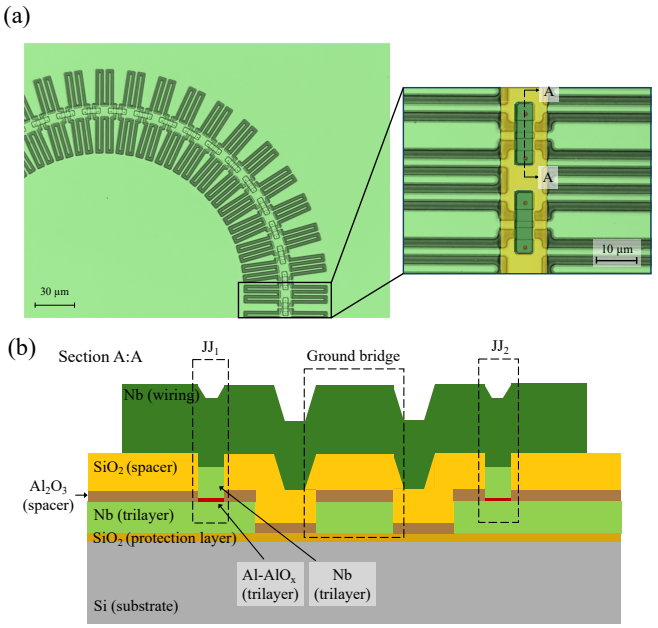

Fig. 6. (a) Microscope image of one of the fabricated devices. The zoom-in image shows the main structures of a unit cell. (b) Cross-section representation of the unit cell, the materials and identifiers of the different layer are stated on the figure. The representation is not drawn to scale.

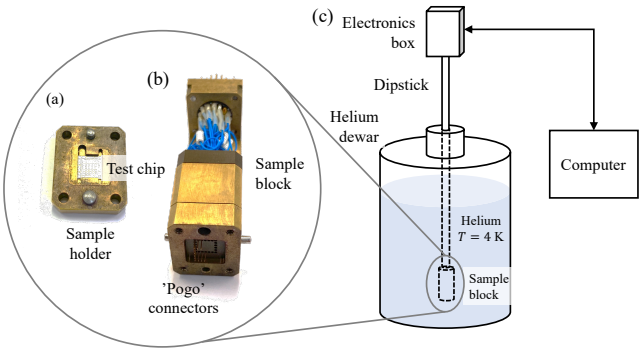

Fig. 7. Experimental setup for the measurement of the current-voltage (IV) relation of our devices. (a) Sample holder where the test device sits. (b) Sample block containing the wiring connections to the chip through 'pogo' pins. (c) Sketch of the dipstick setup.

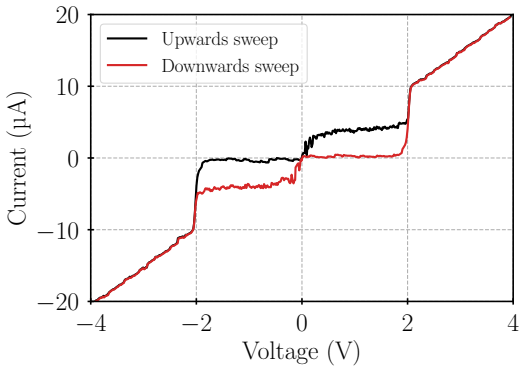

Fig. 8. IV curve measured for our Josephson array device applying an upwards (black) and downwards (red) voltage sweep. The curve shows a gap voltage $V_{\mathrm{gap}} \sim 2\,\mathrm{V}$, and an average normal resistance value of $R_{\mathrm{n}} = 180 \pm 7\,\mathrm{k\Omega}$ — corresponding to an average critical current value of $I_{\mathrm{c}} = 8.43 \pm 0.2\,\mu\mathrm{A}$.

W-band range. Fig. 6 shows the microscope images of the fabricated devices, with a cross-section schematic. The devices were fabricated using the established Nb/Al-AlO_x/Nb trilayer fabrication process. We briefly summarise the fabrication steps here for completion, but for a detailed description of this technique, we refer the reader to [37].

We start with a 280 µm high-resistance ($R > 20,000\,\Omega\cdot$cm) 2-inch silicon wafer where we sputter an ∼70 nm SiO_2 protective layer (Fig. 6(b), dark yellow), required for later steps. The trilayer is then grew using a sputtering machine, with oxidation inside the chamber (Fig. 6(b), light green and red). The oxidation parameters (oxidation time $t_{\mathrm{ox}} = 3\,\mathrm{h}$ and pressure $P_{\mathrm{ox}} = 1.6\,\mathrm{Pa}$) were determined a priori to achieve $J_{\mathrm{c}} = 3.4\,\mathrm{kA/cm^2}$ [38]. Next, we use Reactive Ion Etching (RIE) to remove the trilayer's upper niobium layer within the spacer region. Conventionally, a single photolitography step is used to define the spacer region around the junction. In our case, given the small area of the junctions, we expose the resist in the junction area using an electron beam, and the rest of the device (except the spacer region) using photolithography. After resist development, this exposes the spacer region where the top niobium of the trilayer is removed using RIE. The SiO_2 protection layer avoids etching of the substrate during this step. Next, we evaporate 20 nm Al_2O_3 and sputter 200 nm SiO_2 layer (Fig. 6(b), light yellow and brown) to create the spacer layer. Then, we sputter a ∼ 400 nm niobium top layer interconnecting the junctions (Fig. 6(b), dark green) and layers of titanium and gold are added to the sides of the chip to facilitate the connection to the ground (not shown in Fig. 6). Finally, we mechanically polish the wafer to reduce the thickness to 100 µm.

To DC-screen the fabricated devices, we include a frame structure in our design that allows us to check for open- or short-circuit (to the ground) defects in each device. Fig. 7 shows the experimental setup used for these measurements, consisting of a dipstick where the test chip is mounted on a sample holder and the electrical contacts to the chip are made through 'pogo' pins. The dipstick is dipped into liquid helium to characterise our devices at $T \approx 4\,\mathrm{K}$.

The measured current-voltage (IV) curve of our device is plotted in Fig. 8, which resembles the standard IV curve for an under-dumped Josephson junction (note the hysteresis with voltage sweep), with a gap voltage proportional to the number of junctions in the device $V_{\mathrm{gap,704JJ}} = 704 \times V_{\mathrm{gap,1JJ}} = 704 \times 2.85\,\mathrm{mV} \approx 2\,\mathrm{V}$. The measured data was calibrated following the technique described in the Supplementary Material.

To estimate the critical current of the junctions, we measured the devices' normal resistance value of $R_{\mathrm{n}} = 180 \pm 7\,\mathrm{k\Omega}$. Dividing this value by 704, i.e., the number of junctions in the device, and using the Ambegaokar-Baratoff formula for tunnel junctions [39], we infer the junctions' average

critical current value[4] $I_c = 8.43 \pm 0.2\,\mu A$, substantially smaller than the targeted $I_c = 17\,\mu A$. This result likely originates from a $\sim 50.4\,\%$ reduction of the junction size, in line with measurements performed in other devices fabricated following the same recipe. Assuming $\sim 50.4\,\%$ smaller junctions and an $I_c = 8.43 \pm 0.2\,\mu A$, we re-estimate the cutoff frequency of the device to $f \approx 122\,GHz$ (the implications of this will be further discussed in Sec. V).

IV. RF CHARACTERISATION

This section presents the RF characterisation of the Josephson array device. All the measurements were performed at 1 K, unless otherwise stated.

A. Cryogenic system and mounting technique

The RF characterisations were performed using the cryogenic platform depicted in Fig. 9(a), where a cryocooler is used to cool the system down to 4 K and a helium-4 sorption cooler further decreases the temperature of the cold-plate to 1 K. The system is equipped with four WR-10 waveguide lines, and our device is mounted in a WR-10 waveguide copper split-block interfacing the waveguide channels of the system. The split-block consisted of two curved WR-10 waveguides, interconnected with a groove to accommodate the Josephson-array chip (Fig. 9(b)). The groove has a channel of 300 µm wide and 200 µm deep underneath the chip to suppress possible resonant modes in the substrate. As shown in Fig. 9(b), the device is manually aligned to the groove slot and silver dust-arrester-ground (DAG) paint is applied at the edges of the chip to ground the device.

B. Transmission measurement

The transmission spectrum of our device was measured using the experimental setup presented in Fig. 10(a). The signal from the Vector Network Analyser (VNA) and the pump tone from a signal generator are up-converted with frequency multipliers to the W-band, and combined at room temperature before injecting to the device under test (DUT). Fixed attenuation inside the cryostat reduces the estimated $-68\,dBm$ room temperature thermal noise to $-98\,dBm$, well below the critical current limit for our device $P_{I_c} = -51\,dBm$. Additional variable attenuators outside the cryostat are used to adjust the signal and pump power reaching the DUT. A pair of isolators is connected to the DUT to protect the device from possible power reflections. The output spectrum of the DUT is then amplified using a room temperature amplifier before being down-converted and readout with the VNA.

Fig. 10(b) shows the measured transmission profiles, calibrated with the room temperature transmission data measured through a blank feedthrough line replacing the DUT, for different values of the variable attenuator in the signal path (α_s). We estimate the power at the input of our device of

[4]Note that the the measured switching current underestimates the average junction I_c, likely due to premature and cascade switching dominated by the weakest junctions. We extract the I_c from the normal resistance via the Ambegaokar–Baratoff relation, yielding a more accurate ensemble-average value.

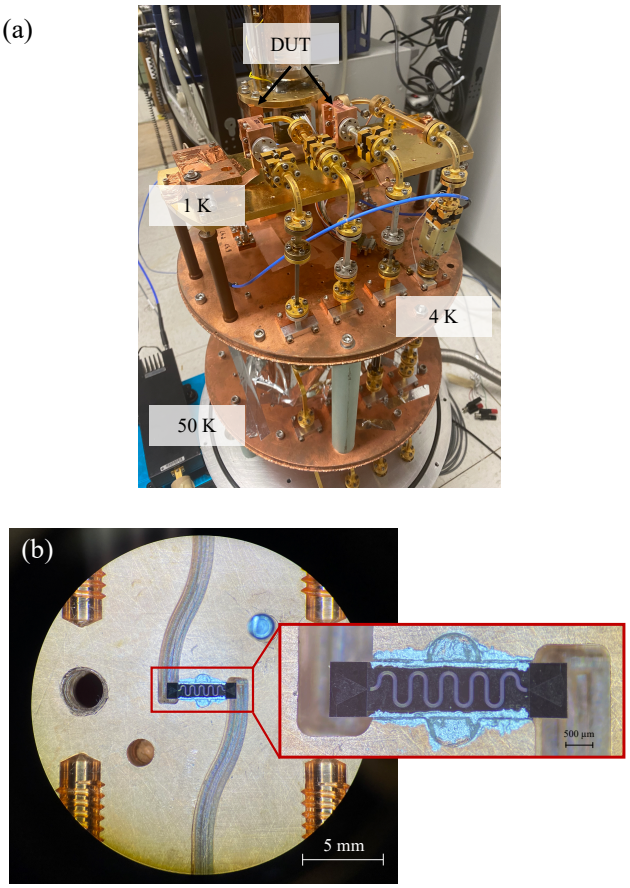

Fig. 9. (a) Cryogenic platform used for the RF measurement of our devices. The devices under tests (DUTs) are mounted at the 1 K stage equipped with waveguide lines. (b) Microscope image of our device mounted in the WR-10 waveguide split-block. The RF signal is coupled in and out of the chip through curved waveguide structures. Zoom-in image: The chip is manually mounted on a groove connecting both waveguides, using silver DAG to connect the CPW ground to the copper block and to hold the device.

$P_{in} = -62$, -52 and $-42\,dBm$ for α_s values of 40, 30 and 20 dB respectively. Assuming an ideal signal coupling into our device, we would expect to observe a flat 0 dB transmission for P_{in} less than –51 dBm, and a sudden drop in transmission for $\alpha_s = 20\,dB$ when the input power exceeds P_{I_c}. However, for all the α_s settings, we observed over 30 dB of unexpected losses with periodic features that cleared up with lower attenuation. These losses could originate from coupling issues and internal loss mechanisms in the device, a detailed discussion is given in Sec. V. As a result of these losses, the actual power in the device for $\alpha_s = 40\,dB$ may be at $-92\,dBm$, close to the room temperature noise level, resulting in a poor SNR. Therefore, when we increase P_{in} by decreasing the attenuation, we couple more energy into our device and the SNR improves as shown in Fig. 10(b). However, due to the quasi-fixed setting of the system, we are unable to further reduce the attenuation beyond 20 dB, hence we could not observe the breaking of superconductivity by exceeding the critical current within our device.

Based on the previous results, we fix $\alpha_s = 20\,dB$, i.e., $P_s \sim$

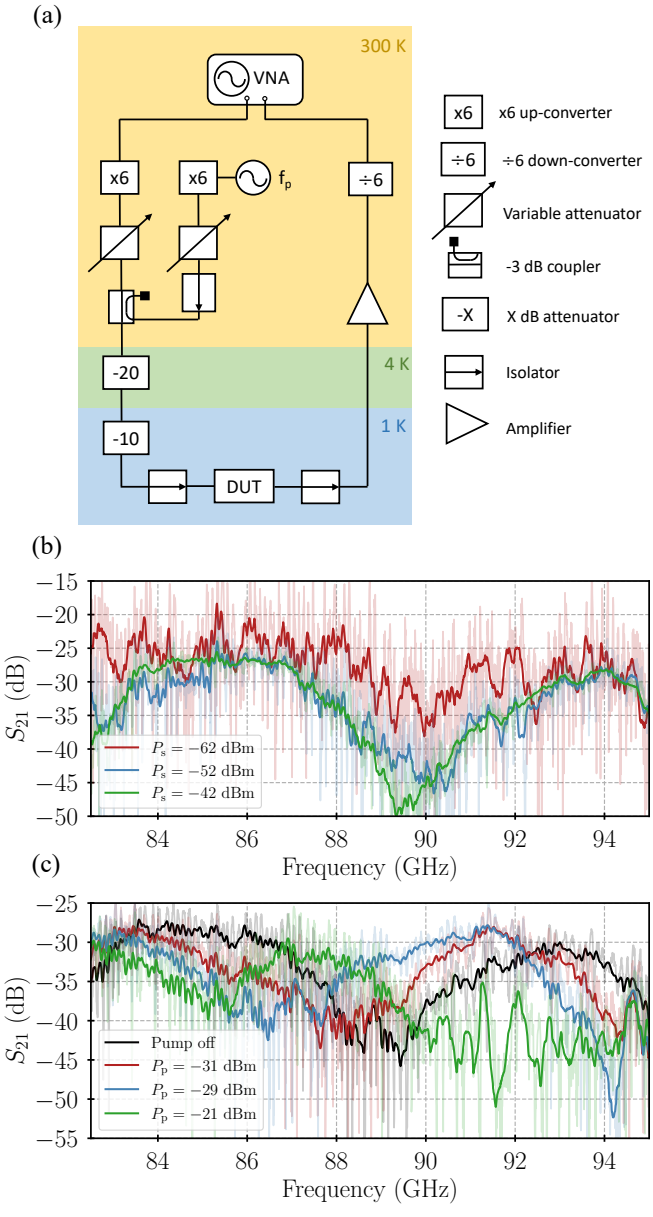

Fig. 10. (a) Experimental setup for the RF transmission measurement. (b) Transmission profile of the device with different applied signal power P_s levels. (c) RF transmission when pumped with different pump power P_p levels. All the values in the legends indicate the estimated power at the input of our device.

-72 dBm at the device after taking into account the 30 dB loss, and apply a pump tone with $f_p = 92$ GHz. We measure the transmission profiles for different values of variable attenuator in the pump path resulting in a pump power $P_p = -61, -59$ and -51 dBm at the input of the device (after loss)[5]. The results are plotted in Fig. 10(c), which clearly show that the periodic features in the transmission profile shift in frequency with increasing pump power. This indicates a change in the phase velocity of the transmission line with pump power, an

[5]The total power coupled into the device is dominated by the pump power in this case, since the signal power is marginal at –72 dBm, hence we quote only the pump power in the text.

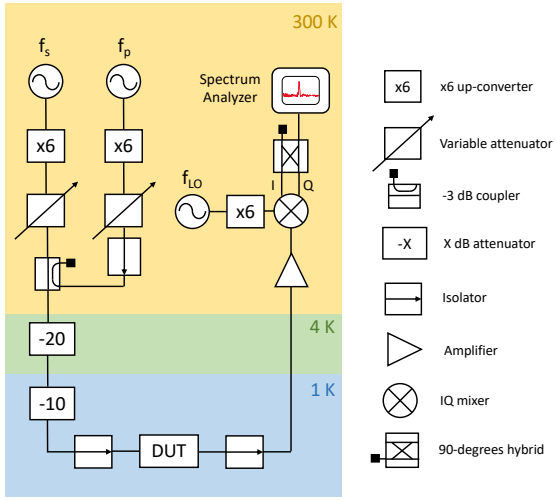

Fig. 11. Experimental setup for the measurement of the 4WM idler. The output signal from the DUT is down-converted to the microwave regime using an IQ-mixer instead of down-converter. A terminated 90-degrees hybrid is used to reject the image band of the mixer, and the down-converted signal is read using a spectrum analyser.

evidence of the nonlinear inductance of the junctions forming the array. Focusing on the regime between 90–94 GHz, we further observed a sudden drop in transmission power for $P_p = -51$ dBm (after loss), suggesting that some of the junction may have transitioned to their normal state, as the input pump power is just above $P_{I_c} = -52$ dBm. Note that the losses distribution accross the array are hard to estimate from the measurements, and could be frequency-dependent, which may explain why a sudden transmission drop is not observed across all the frequencies.

C. Four-wave mixing (4WM) processes

To further confirm the $\chi^{(3)}$ nature of the nonlinear effects, we perform a measurement of four-wave mixing (4WM) by applying both a pump (ω_p) and a signal (ω_s) tone to the device. In the presence of 4WM interactions, an idler tone is expected to be generated at the frequency $\omega_i = 2\omega_p - \omega_s$. The experimental setup, shown in Fig. 11, consists of injecting the two tones into the device under test (DUT), followed by down-conversion to the microwave regime using an IQ mixer in conjunction with a quadrature hybrid. One output port of the hybrid is terminated to suppress the image band of the mixer, while the other port is connected to a spectrum analyser for signal detection.

We search for the idler generation in the 85–85.5 GHz range where the transmission is less lossy. We fix the pump frequency at $f_p = 85.235$ GHz and the local oscillator frequency for the mixer at $f_{LO} = 80$ GHz. The results measured for different signal frequencies, when $\alpha_s = 50$ dB and $\alpha_p = 0$ dB, are plotted in Fig. 12(a)-(c). In addition to the signal and pump, we notice two spurious tones from the pump that are fixed in frequency around the pump, which originated from the synthesiser used to generate the pump tone. Apart from this,

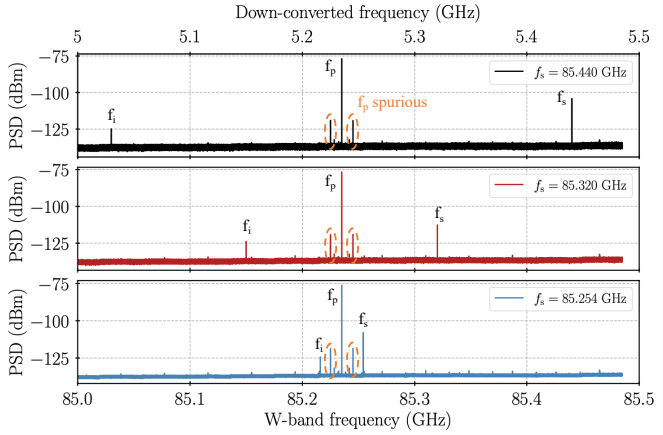

Fig. 12. Power spectrum density (PSD) measured using the setup in Fig. 11 with the setting $\alpha_s = 50\,\text{dB}$, $\alpha_p = 0\,\text{dB}$, $f_p = 85.235\,\text{GHz}$ and $f_{LO} = 80\,\text{GHz}$, when applying a signal tone at (top plot) $f_s = 85.44\,\text{GHz}$, (center plot) $f_s = 85.32\,\text{GHz}$ and (bottom plot) $f_s = 85.254\,\text{GHz}$. The two tones around the pump is associated the frequency synthesiser generating the pump and LO tones. An idler tone at $\omega_i = 2\omega_p - \omega_s$ appears for all the measured signal frequencies, as expected.

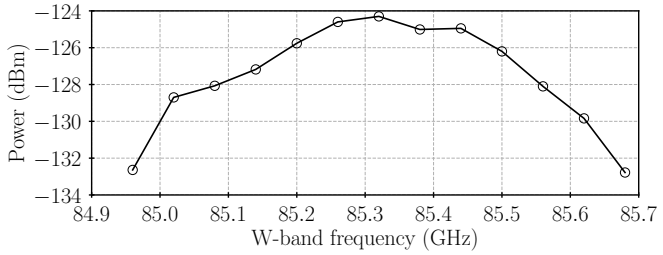

Fig. 13. Measured power of the idler tone for $\alpha_p = 0\,\text{dB}$, $\alpha_s = 50\,\text{dB}$ and $f_p = 85.235\,\text{GHz}$ when sweeping the signal frequency. The x-axis corresponds to the W-band frequency of the idler.

we can clearly see that an idler tone is always generated[6] at $\omega_i = 2\omega_p - \omega_s$. This 4WM process demonstrates the expected χ^3 nonlinearity of the Josephson array in the W-band.

To further confirm that the observed idler tone is indeed generated from our device, we re-ran our experiment by connecting the output of the –3 dB coupler to the input of the readout amplifier (bypassing the cryogenic stages including the DUT), via an extra 30 dB room temperature attenuator to replicate the attenuation setting inside the fridge. Using the same f_p, f_s and f_{LO} as before, we adjust the pump and signal powers i.e., $50 < \alpha_s < 70\,\text{dB}$ and $10 < \alpha_p < 28\,\text{dB}$, and no idler tone is observed.

Finally, in Fig.13, we fix $\alpha_s = 50\,\text{dB}$, $\alpha_p = 0\,\text{dB}$, and $f_p = 85.235\,\text{GHz}$, then we sweep the signal frequency and record the idler frequency and amplitude read from the spectrum analyser. From the plot, we see that the measured idler amplitude reaches higher values around the pump frequency, where the phase-matching condition that maximises the 4WM process is optimal. Although the Josephson array design should support the generation of signal gain, we did not observe this effect likely due to the unexpected high losses in the device. Nevertheless, these idler measurements clearly show the prospects of developing $\chi^{(3)}$ nonlinear metamaterial lines required for operating JTWPAs at high frequency in the mm-wave frequency range.

[6]The reduced idler amplitude compared with the signal is an expected outcome in a lossy transmission line. As the signal propagates, attenuation reduces its strength, which in turn lowers the efficiency of idler generation.

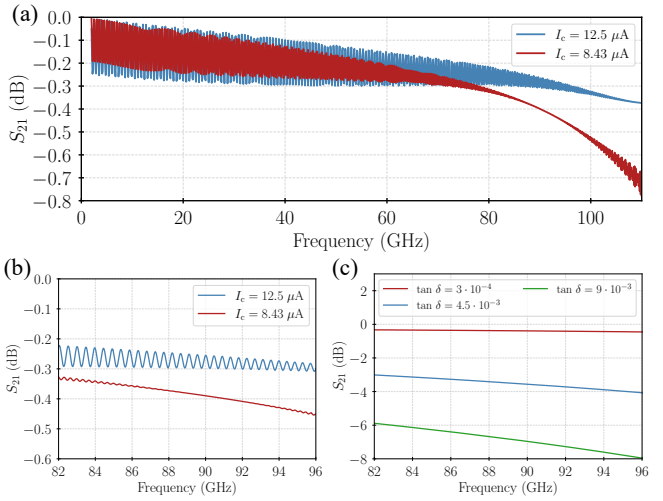

Fig. 14. (a) Calculated transmission with frequency of the Josephson array for the targeted (blue) and measured (red) I_c value. Both calculations assume $\tan\delta = 3 \cdot 10^{-4}$ for the SiO_2 layer. (b) Zoom-in around 90 GHz. (c) Transmission around 90 GHz calculated with $I_c = 8.43\,\mu\text{A}$ for different values of $\tan\delta$ for the SiO_2 layer. The blue curve shows the most realistic value of $\tan\delta$.

V. Losses Discussion

The unexpected losses observed in Fig. 10 prompted a more detailed analysis. A natural explanation could be the reduced measured I_c of the junctions, which lowers the cutoff frequency of the array, hence increasing the losses in the W-band. To investigate this, we re-simulated the unit cell in Ansys HFSS using the measured value of $I_c = 8.43\,\mu\text{A}$, and cascaded the response to obtain the theoretical transmission profile of the full array. Fig. 14(a) compares the simulated transmission of the original design unpumped (blue) with that of the updated model using the measured I_c unpumped (red). In both cases, the observed oscillations arise from the frequency-dependent impedance of the array, leading to mismatch with the simulation ports. Note that the original design was optimised to match $Z_0 = 70\,\Omega$ around 90 GHz when pumped, therefore, the larger impedance mismatch compared to the updated model. A zoomed-in view of the transmission near 90 GHz is shown in Fig. 14(b). While the reduced I_c does result in higher losses, the effect is relatively minor, on the order of only 0.4 dB at 90 GHz.

In our initial simulations, we assumed a loss tangent of $\tan\delta = 3 \cdot 10^{-4}$ for the SiO_2 dielectric layer. However, recent measurements on devices fabricated using the same process indicate a significantly higher value of $\tan\delta = 4.5 \cdot 10^{-3}$. Due to the number of ground bridges utilised in our array, the dielectric losses could be significant. To assess the impact of this higher loss tangent, we fixed the critical current at $I_c = 8.43\,\mu\text{A}$ (measured value) and re-simulated the unit

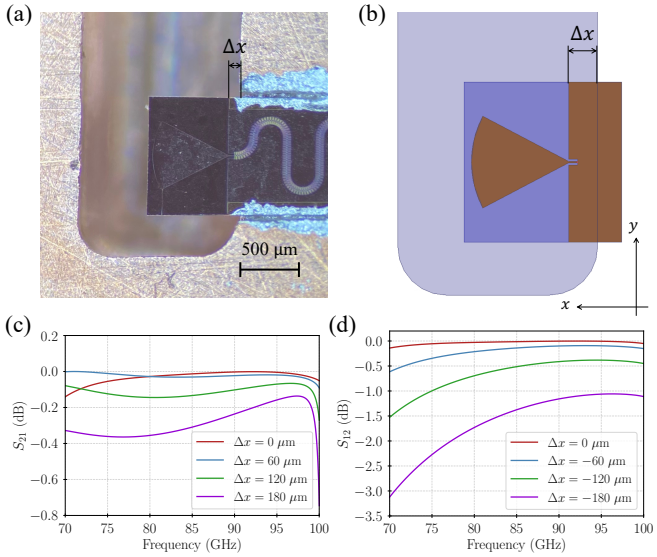

Fig. 15. (a) Image of the probe antenna misalignment under the microscope. (b) Top view of the probe antenna Ansys® HFSS model including the misalignment. (c) S_{21} results of the input probe antenna simulation for different values of Δx. (d) S_{12} results of the output probe antenna simulation for different values of Δx.

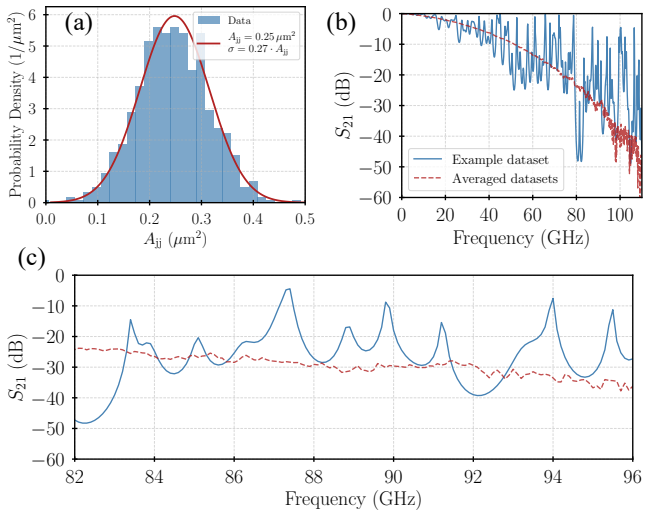

Fig. 16. Analysis of the junction's area spread across the array. (a) Histogram of representative dataset with 704 junctions where A_{jj} follows a normal distribution centre at $A_{jj,0} = 0.25\,\mu m^2$ and standard deviation of $\sigma = 0.27 \cdot A_{jj,0}$. (b) Calculated S_{21} of the array using the dataset in (a) (blue solid line), and the averaged value for 2,000 different datasets with $A_{jj,0} = 0.25\,\mu m^2$ and $\sigma = 0.27 \cdot A_{jj,0}$ (red dotted line). (c) Zoom-in around 90 GHz.

cell for various values of $\tan\delta$. The resulting transmission curves for the full array are shown in Fig. 14(c). For the more realistic value of $\tan\delta = 4.5 \cdot 10^{-3}$ (blue), we observe a substantial increase in insertion loss, reaching approximately 4 dB at 90 GHz. When $\tan\delta$ is doubled (green), the losses rise further to around 6.5 dB. These results highlight that, despite efforts to limit dielectric involvement, dielectric losses still have a significant impact on device performance and should be carefully considered in future designs.

The measured critical current of $I_c = 8.43\,\mu A$ also affects the characteristic impedance of the transmission line, increasing it from the original design value of $70\,\Omega$ to approximately $88\,\Omega$. This change influences the impedance matching and thereby alters the coupling efficiency of the probe antennas. Additionally, inspection of the device under a microscope (Fig. 15(a)) reveals a slight misalignment of the chip within its mounting groove. This misalignment displaces the input and output probe antennas by a distance Δx from their optimal coupling positions. From the image, we estimate $\Delta x \approx +120\,\mu m$ for the input, resulting in an equivalent displacement in the opposite direction for the output antenna i.e., $\Delta x \approx -120\,\mu m$. To evaluate the effect of this displacement, we used our Ansys® HFSS model of the probe antenna (Fig. 15(b)) and simulated the antenna performance with the updated array impedance of $Z_0 = 88\,\Omega$. In our simulations, we define the waveguide as port 1 and the CPW port as port 2. Fig. 15(c)&(d) plot the transmission profile of the input antenna (S_{21}) and the output antenna (S_{12}) for different Δx values respectively. A displacement of $\Delta x = +120\,\mu m$ at the input ($\Delta x = -120\,\mu m$ at the output) leads to an additional coupling loss of approximately 0.1 dB at 90 GHz (0.5 dB at the output). These findings indicate that mechanical misalignments contribute to the coupling losses, although they are unlikely to be the main source of losses in our device.

The spread in the junction area A_{jj} may also introduce unanticipated losses. Variations in A_{jj} along the transmission line lead to corresponding changes in the junction capacitance C_j and inductance L_j, thereby affecting the cutoff frequency and impedance. These fluctuations can cause impedance mismatches, resulting in signal reflections and degradation of the transmission characteristics, more importantly reducing the cutoff frequency. To investigate this effect, we generated a random dataset of 704 junctions, with A_{jj} following a normal distribution centered at $A_{jj,0} = 0.25\,\mu m^2$ — the estimated junction area based on the IV curve measurements — and a standard deviation $\sigma = x \cdot A_{jj,0}$, where x characterises the degree of spread. A histogram of one such dataset with $x = 0.27$ is shown in Fig. 16(a). Using this distribution, we calculated the corresponding circuit parameters and constructed the unit cell `ABCD` matrix assuming the design value $C_s = 6.5\,fF$. These `ABCD` matrices were then cascaded and converted into S-parameters to evaluate the transmission of the entire array.

The blue solid line in Fig. 16(b)&(c) show the corresponding transmission response, S_{21}, for the dataset presented in Fig. 16(a). The S_{21} profile reveals pronounced oscillations that arise from variations in the A_{jj} distribution — consistent with the features observed in our measured device. By averaging the transmission across 2,000 different datasets, we obtain the smoother response shown as the red dashed line in Fig. 16(b)&(c). This result demonstrates that an area spread of $\sigma = 0.27 \cdot A_{jj,0}$ yields an average insertion loss of approximately 30 dB around 90 GHz, in agreement with our experimental observations.

Other potential sources of losses include the presence of two-level system (TLS) losses arising from the dielectric spacer layer in the device. However, TLS-related losses are

typically temperature-dependent and prominent only at low temperatures. In our case, we observe no significant difference in device behaviour between $4\,\mathrm{K}$ and $1\,\mathrm{K}$, suggesting TLS losses are not the dominant mechanism. Another possibility is the presence of trapped magnetic flux, which can introduce excess dissipation. However, this would likely lead to cooldown-dependent variations in transmission characteristics, which we have not observed across repeated measurements. Finally, the poor electrical grounding of the chip due to an insufficient amount of silver DAG could also deteriorate the transmission. However, this effect is difficult to quantify quantitatively.

To conclude, although we have analysed the various potential sources of loss individually, it is important to note that these mechanisms can act concurrently within the device, collectively contributing to the measured transmission profile. Based on our analysis, the dominant contributions to the observed losses are most likely the dielectric losses associated with the ground bridges and the variation in junction area across the array. These findings highlight the critical importance of ensuring uniformity in the junction area, particularly when the device operates near its cutoff frequency, as is the case in our design.

VI. Conclusion

The third-order nonlinearity ($\chi^{(3)}$) of a Josephson array is the key mechanism enabling parametric amplification in a bare-junction Josephson Travelling-Wave Parametric Amplifier (JTWPA). In this work, we have investigated the primary design constraints for operating JTWPAs in the W-band, using a Josephson array model. This analysis led to the design of a Josephson array tailored for W-band operation, with a targeted cutoff frequency around $180\,\mathrm{GHz}$. The array, consisting of 704 Nb/Al-AlO_x/Nb junctions with a designed critical current of $I_\mathrm{c} = 17\,\mu\mathrm{A}$, was subsequently fabricated. However, DC characterisation of the fabricated array yielded a lower value of $I_\mathrm{c} = 8.43 \pm 0.2\,\mu\mathrm{A}$, likely due to a $50.4\,\%$ reduction in junction area caused by side-wall oxidation during fabrication. RF measurements revealed approximately $30\,\mathrm{dB}$ of loss. Further analysis suggests the effect of the junction area spread across the array and the dielectric losses from the ground bridges as the main contributors to the losses. Despite these losses, we observed clear evidence of $\chi^{(3)}$ nonlinearity through the generation of a four-wave mixing idler around $85.25\,\mathrm{GHz}$. These results demonstrate the feasibility of creating nonlinear transmission lines operating in the W-band, paving the way for the development of novel millimetre-wave devices based on Josephson junction technology.

Acknowledgments

The authors would like to thank Farzad Faramarzi and Sasha Sypkens for the useful discussions during the RF characterisation of the devices. This research was supported by the United Kingdom (UK) Science and Technology Facility Council (STFC) under the Quantum for Science Grant (ST/Y004973/1), and the European Research Council (ERC) under the European Union's Horizon 2020 research and innovation programme with grant agreement No. [803862] (Project [SPA4AstroQIT]). J. Navarro Montilla's D.Phil. studentship is supported by the UK STFC and the Foley-Bejar Scholarship from the Balliol College, Oxford. For the purpose of Open Access, the author has applied a CC BY public copyright licence to any Author Accepted Manuscript version arising from this submission.

References

[1] H. Kim, G. Jang, S. Jin, D. Shin, H.-J. Shin, J. Luo, I. Siddiqi, Y. Kim, H. H. Yoon, and L. B. Nguyen, "Josephson junctions in the age of quantum discovery," 2025. [Online]. Available: https://arxiv.org/abs/2505.12724

[2] C. A. Hamilton, C. Burroughs, and K. Chieh, "Operation of nist josephson array voltage standards." *J Res Natl Inst Stand Technol*, vol. 95, no. 3, pp. 219–235, May-Jun 1990.

[3] S. V. Uchaikin, J. Kim, C. Kutlu, B. I. Ivanov, J. Kim, A. F. van Loo, Y. Nakamura, S. Ahn, S. Oh, M. Ko, and Y. K. Semertzidis, "Josephson parametric amplifier based quantum noise limited amplifier development for axion search experiments in capp," 2024. [Online]. Available: https://arxiv.org/abs/2406.07899

[4] Z. R. Lin, K. Inomata, W. D. Oliver, K. Koshino, Y. Nakamura, J. S. Tsai, and T. Yamamoto, "Single-shot readout of a superconducting flux qubit with a flux-driven Josephson parametric amplifier," *Applied Physics Letters*, vol. 103, no. 13, p. 132602, 09 2013. [Online]. Available: https://doi.org/10.1063/1.4821822

[5] P. Krantz, A. Bengtsson, M. Simoen, S. Gustavsson, V. Shumeiko, W. D. Oliver, C. M. Wilson, P. Delsing, and J. Bylander, "Single-shot read-out of a superconducting qubit using a josephson parametric oscillator," *Nature Communications*, vol. 7, no. 1, p. 11417, 2016. [Online]. Available: https://doi.org/10.1038/ncomms11417

[6] T. White, A. Opremcak, G. Sterling, A. Korotkov, D. Sank, R. Acharya, M. Ansmann, F. Arute, K. Arya, J. C. Bardin, A. Bengtsson, A. Bourassa, J. Bovaird, L. Brill, B. B. Buckley, D. A. Buell, T. Burger, B. Burkett, N. Bushnell, Z. Chen, B. Chiaro, J. Cogan, R. Collins, A. L. Crook, B. Curtin, S. Demura, A. Dunsworth, C. Erickson, R. Fatemi, L. F. Burgos, E. Forati, B. Foxen, W. Giang, M. Giustina, A. Grajales Dau, M. C. Hamilton, S. D. Harrington, J. Hilton, M. Hoffmann, S. Hong, T. Huang, A. Huff, J. Iveland, E. Jeffrey, M. Kieferová, S. Kim, P. V. Klimov, F. Kostritsa, J. M. Kreikebaum, D. Landhuis, P. Laptev, L. Laws, K. Lee, B. J. Lester, A. Lill, W. Liu, A. Locharla, E. Lucero, T. McCourt, M. McEwen, X. Mi, K. C. Miao, S. Montazeri, A. Morvan, M. Neeley, C. Neill, A. Nersisyan, J. H. Ng, A. Nguyen, M. Nguyen, R. Potter, C. Quintana, P. Roushan, K. Sankaragomathi, K. J. Satzinger, C. Schuster, M. J. Shearn, A. Shorter, V. Shvarts, J. Skruzny, W. C. Smith, M. Szalay, A. Torres, B. W. K. Woo, Z. J. Yao, P. Yeh, J. Yoo, G. Young, N. Zhu, N. Zobrist, Y. Chen, A. Megrant, J. Kelly, and O. Naaman, "Readout of a quantum processor with high dynamic range Josephson parametric amplifiers," *Applied Physics Letters*, vol. 122, no. 1, p. 014001, 01 2023. [Online]. Available: https://doi.org/10.1063/5.0127375

[7] L. Planat, R. Dassonneville, J. P. Martínez, F. Foroughi, O. Buisson, W. Hasch-Guichard, C. Naud, R. Vijay, K. Murch, and N. Roch, "Understanding the saturation power of josephson parametric amplifiers made from squid arrays," *Phys. Rev. Appl.*, vol. 11, p. 034014, Mar 2019. [Online]. Available: https://link.aps.org/doi/10.1103/PhysRevApplied.11.034014

[8] T. Roy, S. Kundu, M. Chand, A. M. Vadiraj, A. Ranadive, N. Nehra, M. P. Patankar, J. Aumentado, A. A. Clerk, and R. Vijay, "Broadband parametric amplification with impedance engineering: Beyond the gain-bandwidth product," *Applied Physics Letters*, vol. 107, no. 26, p. 262601, 12 2015. [Online]. Available: https://doi.org/10.1063/1.4939148

[9] J. Aumentado, "Superconducting parametric amplifiers: The state of the art in josephson parametric amplifiers," *IEEE Microwave Magazine*, vol. 21, no. 8, pp. 45–59, 2020.

[10] B. Ho Eom, P. K. Day, H. G. LeDuc, and J. Zmuidzinas, "A wideband, low-noise superconducting amplifier with high dynamic range," *Nature Physics*, vol. 8, no. 8, pp. 623–627, 2012. [Online]. Available: https://doi.org/10.1038/nphys2356

[11] C. Macklin, K. O'Brien, D. Hover, M. E. Schwartz, V. Bolkhovsky, X. Zhang, W. D. Oliver, and I. Siddiqi, "A near–quantum-limited josephson traveling-wave parametric amplifier," *Science*, vol. 350, no. 6258, pp. 307–310, 2015. [Online]. Available: https://www.science.org/doi/abs/10.1126/science.aaa8525

[12] L. Planat, A. Ranadive, R. Dassonneville, J. Puertas Martínez, S. Léger, C. Naud, O. Buisson, W. Hasch-Guichard, D. M. Basko, and N. Roch, "Photonic-crystal josephson traveling-wave parametric amplifier," *Phys. Rev. X*, vol. 10, p. 021021, Apr 2020. [Online]. Available: https://link.aps.org/doi/10.1103/PhysRevX.10.021021

[13] A. Ranadive, M. Esposito, L. Planat, E. Bonet, C. Naud, O. Buisson, W. Guichard, and N. Roch, "Kerr reversal in josephson meta-material and traveling wave parametric amplification," *Nature Communications*, vol. 13, no. 1, p. 1737, 2022. [Online]. Available: https://doi.org/10.1038/s41467-022-29375-5

[14] N. Klimovich, P. Day, S. Shu, B. H. Eom, H. Leduc, and A. Beyer, "Demonstration of a quantum noise limited traveling-wave parametric amplifier," 2023.

[15] F. Faramarzi, R. Stephenson, S. Sypkens, B. H. Eom, H. LeDuc, and P. Day, "A 4-8 ghz kinetic inductance travelling-wave parametric amplifier using four-wave mixing with near quantum-limit noise performance," 2024.

[16] J. Heinsoo, C. K. Andersen, A. Remm, S. Krinner, T. Walter, Y. Salathé, S. Gasparinetti, J.-C. Besse, A. Potočnik, A. Wallraff, and C. Eichler, "Rapid high-fidelity multiplexed readout of superconducting qubits," *Phys. Rev. Appl.*, vol. 10, p. 034040, Sep 2018. [Online]. Available: https://link.aps.org/doi/10.1103/PhysRevApplied.10.034040

[17] J. M. Navarro and B.-K. Tan, "Optimising the design of a broadband Josephson junction TWPA for axion dark matter search experiments," in *Quantum Technology: Driving Commercialisation of an Enabling Science II*, M. J. Padgett, K. Bongs, A. Fedrizzi, and A. Politi, Eds., vol. 11881, International Society for Optics and Photonics. SPIE, 2021, p. 1188115. [Online]. Available: https://doi.org/10.1117/12.2601382

[18] C. Bartram, T. Braine, R. Cervantes, N. Crisosto, N. Du, G. Leum, P. Mohapatra, T. Nitta, L. J. Rosenberg, G. Rybka, J. Yang, J. Clarke, I. Siddiqi, A. Agrawal, A. V. Dixit, M. H. Awida, A. S. Chou, M. Hollister, S. Knirck, A. Sonnenschein, W. Wester, J. R. Gleason, A. T. Hipp, S. Jois, P. Sikivie, N. S. Sullivan, D. B. Tanner, E. Lentz, R. Khatiwada, G. Carosi, C. Cisneros, N. Robertson, N. Woollett, L. D. Duffy, C. Boutan, M. Jones, B. H. LaRoque, N. S. Oblath, M. S. Taubman, E. J. Daw, M. G. Perry, J. H. Buckley, C. Gaikwad, J. Hoffman, K. Murch, M. Goryachev, B. T. McAllister, A. Quiskamp, C. Thomson, M. E. Tobar, V. Bolkhovsky, G. Calusine, W. Oliver, and K. Serniak, "Dark matter axion search using a Josephson Traveling wave parametric amplifier," *Review of Scientific Instruments*, vol. 94, no. 4, p. 044703, 04 2023. [Online]. Available: https://doi.org/10.1063/5.0122907

[19] K. Ramanathan, N. Klimovich, R. Basu Thakur, B. H. Eom, H. G. Leduc, S. Shu, A. D. Beyer, and P. K. Day, "Wideband direct detection constraints on hidden photon dark matter with the qualiphide experiment," *Phys. Rev. Lett.*, vol. 130, p. 231001, Jun 2023. [Online]. Available: https://link.aps.org/doi/10.1103/PhysRevLett.130.231001

[20] J. N. Montilla and B.-K. Tan, "Design of high compression point Josephson junction travelling wave parametric amplifiers for readout of millimetre and sub-millimetre astronomical receivers," in *Millimeter, Submillimeter, and Far-Infrared Detectors and Instrumentation for Astronomy XI*, J. Zmuidzinas and J.-R. Gao, Eds., vol. 12190, International Society for Optics and Photonics. SPIE, 2022, p. 1219030. [Online]. Available: https://doi.org/10.1117/12.2628992

[21] N. Zobrist, B. H. Eom, P. Day, B. A. Mazin, S. R. Meeker, B. Bumble, H. G. LeDuc, G. Coiffard, P. Szypryt, N. Fruitwala, I. Lipartito, and C. Bockstiegel, "Wide-band parametric amplifier readout and resolution of optical microwave kinetic inductance detectors," *Applied Physics Letters*, vol. 115, no. 4, p. 042601, 07 2019. [Online]. Available: https://doi.org/10.1063/1.5098469

[22] D. Fraudet, I. Snyman, D. M. Basko, S. Léger, T. Sépulcre, A. Ranadive, G. L. Gal, A. Torras-Coloma, S. Florens, and N. Roch, "Direct detection of down-converted photons spontaneously produced at a single josephson junction," 2024.

[23] M. Esposito, A. Ranadive, L. Planat, S. Leger, D. Fraudet, V. Jouanny, O. Buisson, W. Guichard, C. Naud, J. Aumentado, F. Lecocq, and N. Roch, "Observation of two-mode squeezing in a traveling wave parametric amplifier," *Phys. Rev. Lett.*, vol. 128, p. 153603, Apr 2022. [Online]. Available: https://link.aps.org/doi/10.1103/PhysRevLett.128.153603

[24] J. Y. Qiu, A. Grimsmo, K. Peng, B. Kannan, B. Lienhard, Y. Sung, P. Krantz, V. Bolkhovsky, G. Calusine, D. Kim, A. Melville, B. M. Niedzielski, J. Yoder, M. E. Schwartz, T. P. Orlando, I. Siddiqi, S. Gustavsson, K. P. O'Brien, and W. D. Oliver, "Broadband squeezed microwaves and amplification with a josephson travelling-wave parametric amplifier," *Nature Physics*, vol. 19, no. 5, pp. 706–713, 2023. [Online]. Available: https://doi.org/10.1038/s41567-022-01929-w

[25] P. Livreri, E. Enrico, D. Vitali, and A. Farina, "Microwave quantum radar using a josephson traveling wave parametric amplifier and a phase-conjugate receiver for a long-distance detection," in *2023 IEEE Radar Conference (RadarConf23)*, 2023, pp. 1–5.

[26] O.Noroozian, "Cycle 5 nrao alma development study report technology development of quantum-limited, ultra-wideband rf amplifiers for alma: A 65-150 ghz test case," Tech. Rep., 2020.

[27] F. Faramarzi, P. Day, J. Glasby, S. Sypkens, M. Colangelo, R. Chamberlin, M. Mirhosseini, K. Schmidt, K. K. Berggren, and P. Mauskopf, "Initial design of a w-band superconducting kinetic inductance qubit," *IEEE Transactions on Applied Superconductivity*, vol. 31, no. 5, pp. 1–5, 2021.

[28] A. V. Anferov, "Millimeter-wave superconducting quantum devices," Ph.D. dissertation, University of Chicago, 2024.

[29] P. K. Day, N. Klimovich, S. Shu, B. Eom, and H. G. LeDuc, "Millimeter-wave superconducting parametric amplifiers based on kinetic inductance," in *Millimeter, Submillimeter, and Far-Infrared Detectors and Instrumentation for Astronomy XI*, J. Zmuidzinas and J.-R. Gao, Eds., vol. PC12190, International Society for Optics and Photonics. SPIE, 2022, p. PC1219009. [Online]. Available: https://doi.org/10.1117/12.2629110

[30] B.-K. Tan, N. Klimovich, R. Stephenson, F. Faramarzi, and P. Day, "Operation of kinetic-inductance travelling wave parametric amplifiers at millimetre wavelengths," *Superconductor Science and Technology*, vol. 37, no. 3, p. 035006, feb 2024. [Online]. Available: https://dx.doi.org/10.1088/1361-6668/ad20fd

[31] A. Fadavi Roudsari, D. Shiri, H. Renberg Nilsson, G. Tancredi, A. Osman, I.-M. Svensson, M. Kudra, M. Rommel, J. Bylander, V. Shumeiko, and P. Delsing, "Three-wave mixing traveling-wave parametric amplifier with periodic variation of the circuit parameters," *Applied Physics Letters*, vol. 122, no. 5, p. 052601, 01 2023. [Online]. Available: https://doi.org/10.1063/5.0127690

[32] L. Planat, "Resonant and traveling-wave parametric amplification near the quantum limit," Ph.D. dissertation, University of Grenoble Alpes, 2020.

[33] C. S. Macklin, "Quantum feedback and traveling-wave parametric amplification in superconducting circuits," Ph.D. dissertation, UniversityofCalifornia,Berkeley, 2015.

[34] "Sonnet software," https://www.sonnetsoftware.com/.

[35] J. Navarro Montilla and B. K. Tan, "Extending the kinetic-inductance travelling wave parametric amplifiers coupled-mode framework to other symmetric nonlinear mediums with χ^3 nonlinearity," *Superconductor Science and Technology*, 2025. [Online]. Available: http://iopscience.iop.org/article/10.1088/1361-6668/ade0f2

[36] "Ansys hfss," https://www.ansys.com/products/electronics/ansys-hfss.

[37] J. N. Montilla, N. Klimovich, A. Barbier, E. F. C. Driessen, and B.-K. Tan, "Parametric amplification in a josephson junction array fabry-pérot cavity," *Physica Scripta*, vol. 100, no. 9, p. 095016, sep 2025. [Online]. Available: https://doi.org/10.1088/1402-4896/ae03f0

[38] J. Navarro Montilla, E. Driessen, A. Barbier, F. Boussaha, C. Chaumont, and B.-K. Tan, "Exploring the limits of the tunnel junction fabrication technique for josephson junctions twpa and the preliminary characterisation results," 2022.

[39] M. Tinkham, *Introduction to superconductivity*. Courier Corporation, 2004.